



# CHORUS

This is the accepted manuscript made available via CHORUS. The article has been published as:

## Defect-driven localization crossovers in MBE-grown La-doped SrSnO<sub>3</sub> films

Tianqi Wang, Laxman Raju Thoutam, Abhinav Prakash, William Nunn, Greg Haugstad, and Bharat Jalan

Phys. Rev. Materials **1**, 061601 — Published 9 November 2017

DOI: [10.1103/PhysRevMaterials.1.061601](https://doi.org/10.1103/PhysRevMaterials.1.061601)

# **Defect-driven Localization Crossovers in MBE-Grown La-doped SrSnO<sub>3</sub> films**

Tianqi Wang<sup>1,§</sup>, Laxman Raju Thoutam<sup>1,§</sup>, Abhinav Prakash<sup>1</sup>, William Nunn<sup>1</sup>, Greg Haugstad<sup>2</sup>  
and Bharat Jalan<sup>1,a</sup>

<sup>1</sup>Department of Chemical Engineering and Materials Science, University of Minnesota - Twin  
Cities, Minneapolis, Minnesota 55455, USA

<sup>2</sup>Characterization Facility, University of Minnesota, Minneapolis MN 55455

<sup>§</sup> Authors contributed equally to this work

<sup>a</sup> Email: [bjalan@umn.edu](mailto:bjalan@umn.edu) (corresponding author)

**Abstract:**

Through systematic control of cation stoichiometry using a hybrid molecular beam epitaxy method, we show a crossover from weak to strong localization of electronic carriers in La-doped  $\text{SrSnO}_3$  films on  $\text{LaAlO}_3(001)$ . We demonstrate that substrate-induced dislocations in these films can have a strong influence on the electron phase coherence length resulting in 2D to 3D weak localization crossover. We discuss the correlation between electronic transport, and defects associated with non-stoichiometry and dislocations.

Doped alkaline-earth stannates ( $\text{BaSnO}_3$  and  $\text{SrSnO}_3$ ) with high room temperature conductivity, and wide bandgap are of significant interest for transparent conductors, and high-power electronic device applications in addition to as channel materials in oxide-based heterostructures.<sup>1-6</sup> Historically, perovskite oxides have shown poor room temperature mobility owing in part to their band structures, and in part to the presence of intrinsic and extrinsic defects. It was only recently that these materials have witnessed emerging interest for room temperature electronics due to the discovery of high room temperature mobility in bulk single crystals<sup>1, 2</sup> as well as in thin films of doped  $\text{BaSnO}_3$  (BSO)<sup>7-11</sup>. Doped  $\text{SrSnO}_3$  (SSO), on the other hand, is relatively less explored.

Room temperature phase of SSO has an orthorhombic perovskite structure (space group  $Pbnm$ ) with lattice parameters of  $a_0 = 5.709 \text{ \AA}$ ,  $b_0 = 5.703 \text{ \AA}$  and  $c_0 = 8.065 \text{ \AA}$  and a wide bandgap of 3.9 - 4.5 eV.<sup>12-14</sup> Electronic band structure of SSO is derived from Sn  $5s$  and O  $2p$  bands, where predominantly Sn  $5s$  states form the conduction band minima thus offering the benefit of low electron effective mass as compared to  $d$ -band perovskite.<sup>14-16</sup> Moreover, the wider bandgap and smaller lattice parameter of SSO than that of BSO (and therefore, better lattice-matched to many commercially available substrates) makes it a promising material with direct relevance to applications such as high-power devices and transparent electronics. In this context, understanding the role of specific defects on electronic properties of SSO is of significant interest. There are a number of open questions however that are yet to be explored in SSO including the optimal choice of dopant ions, and the relative importance of phonon, ionized impurity scattering including those from point defects, and dislocations. Dislocation and point defect scattering are more significant in thin films due to lattice mismatch between films and substrates, and influence of the growth parameters on film's stoichiometry, respectively. Prior

works have focused on the synthesis of SSO films using sol-gel method<sup>17</sup>, pulsed laser deposition (PLD)<sup>18-21</sup>, and sputtering<sup>22</sup>. More recently, low energy MBE approach has been demonstrated to yield structurally high quality SSO films but was unsuccessful in producing conducting films despite doping with large amount of La.<sup>12</sup> Theoretically, La is predicted to be a shallow donor in SSO,<sup>16</sup> raising questions on the intrinsic electronic properties of SSO.

To investigate the intrinsic electronic properties of SSO and to identify the roles of cation stoichiometry and dislocations on the electronic transport in doped SSO films, this letter focuses on the hybrid MBE growth of La doped-SSO films and temperature-dependent magneto-transport properties providing numerous insights into the role of intrinsic defects on localization physics in SSO films.

We begin by first discussing the structural properties of SSO films on LAO(001), which are critical in establishing a credible case for the electronic properties. Figure 1a shows time-dependent RHEED intensity oscillations during the growth of a representative stoichiometric SSO film (Sr/Sn BEP ratio =  $8.6 \times 10^{-3}$ ) indicating that films grew in an atomic layer-by-layer fashion. The inset shows a streaky RHEED pattern after growth with  $\frac{1}{2}$ -order reflections along  $[100]_{\text{LAO}}$  azimuth indicating smooth surface morphology. Figure 1b shows a wide-angle x-ray diffraction (WAXRD) scan for La-doped SSO(45 nm)/undoped SSO(9 nm)/LAO(001) grown with the same cation flux ratio revealing phase pure film with an expanded out-of-plane lattice parameter ( $a_{\text{OP}}$ ) of  $4.075 \text{ \AA} \pm 0.002 \text{ \AA}$ . This  $a_{\text{OP}}$  value is higher than the pseudo-cubic lattice parameter ( $c = 4.035 \text{ \AA}$ ) of bulk SSO indicating this film contains either non-stoichiometric/structural defects/doping or has residual in-plane (biaxial) strain due to incomplete strain relaxation. To examine the role of strain, we performed an off-axis RSM scan around (103) reflection of the same film revealing an out-of-plane lattice parameter value of

4.075 Å ± 0.002 Å, consistent with the results of on-axis WAXRD scans, and an in-plane lattice parameter value of 4.008 ± 0.002 Å (Fig. 1c). We calculate the unstrained lattice parameter of SSO film using the following equation:

$$a_{\text{unstrained}} = \frac{2\nu a + (1-\nu)a_{\perp}}{1+\nu}$$

where  $\nu$  is the Poisson's ratio for bulk SSO (set to a theoretical value of 0.192<sup>23</sup>), and  $a$  and  $a_{\perp}$  are the experimental values of the in-plane and the out-of-plane lattice parameters, respectively, determined from the RSM. The value of  $a_{\text{unstrained}}$  was calculated to be 4.053 Å ± 0.002 Å, which is about 0.44% higher than the bulk pseudocubic value as one would expect for a nominally stoichiometric composition without any doping. We attribute this increase either to the presence of La-dopants in these films or to the error in the theoretical value of Poisson's ratio. We also note that cation non-stoichiometry may also yield a similar increase in the lattice parameter. To this end, to directly examine the film's cation stoichiometry, we employed the Rutherford Backscattering Spectrometry (RBS) measurements, which confirmed nominally stoichiometric composition for these films (see Fig. S1).<sup>24</sup>

As a more sensitive measure of point defects and non-stoichiometry-related defects, we performed electronic transport measurements on La-doped SSO films with a fixed La dopant concentration but varying Sr/Sn ratio. La was used as an n-type dopant and its concentration in the films was kept nominally constant by fixing La-cell temperature and the growth rate. It is expected that non-stoichiometric defects such as Sr- or Sn-vacancies will compensate for electrons resulting in lower carrier density and mobility similar to what has been shown for La-doped BSO films.<sup>25, 26</sup> Figure S1 shows RBS measurements and simulations of La-doped SSO(45 nm)/undoped SSO(9 nm)/LAO(001) grown at Sr/Sn BEP ratio between  $5.7 \times 10^{-3}$  and  $12.0 \times 10^{-3}$  demonstrating a systematic change in film's Sr/Sn ratio with changing growth

conditions.<sup>24</sup> Importantly, films grown with Sr/Sn BEP ratios of  $7.8 \times 10^{-3}$  and  $8.6 \times 10^{-3}$  showed nominally identical cation stoichiometry with Sr/Sn RBS ratio of  $1.01 \pm 0.02$  and  $0.98 \pm 0.02$ , respectively. Figure 2a shows T-dependent resistivity ( $\rho$ ) of these films indicated by their Sr/Sn ratio determined from the RBS measurements. Results from stoichiometric La-doped SSO(40 nm)/undoped SSO(8 nm) films grown on GSO(110) are also included. The corresponding room-temperature values of electron density ( $n$ ), and mobility ( $\mu$ ) of these films are shown in Fig. 2b and 2c respectively, as a function of Sr/Sn ratio determined from the RBS. We first discuss the electronic transport of La-doped SSO films grown on LAO(001). Films grown with Sr/Sn BEP ratios of  $7.8 \times 10^{-3}$  (Sr/Sn RBS ratio =  $1.01 \pm 0.02$ ) and  $8.6 \times 10^{-3}$  (Sr/Sn RBS ratio =  $0.98 \pm 0.02$ ) yielded identical room temperature  $\rho$  values  $\sim 5.5$  m $\Omega$ -cm,  $n \sim 5.5 \times 10^{19}$  cm $^{-3}$ , and  $\mu \sim 22$  cm $^2$ V $^{-1}$ s $^{-1}$  (Fig. 2a-c) suggesting nominally identical composition, in agreement with the results of RBS measurement (Fig. S1).<sup>24</sup> These results revealed that there exists an adsorption-controlled MBE growth window (marked by green shaded region in Fig. 2b and 2c), i.e. a range of Sr/Sn BEP ratios where only stoichiometric SSO films grow. We attribute this behavior to the high volatility of HMDT precursor, similar to what has been demonstrated for BSO films.<sup>25</sup> With increasing non-stoichiometry, both  $n$  and  $\mu$  decreased suggesting cation non-stoichiometry can cause carrier localization and enhance scattering regardless of whether they were Sr- or Sn-vacancies. These results, while attesting to the excellent composition control afforded by the hybrid MBE approach, suggest that the observed and unexplained non-conducting behavior of MBE-grown La doped-SSO films may be due to the presence of non-stoichiometric defects.<sup>12</sup> The presence of non-stoichiometry-related defects also revealed significant influence on the low temperature resistivity behavior. Figure 2a shows an upturn in  $\rho$  at low temperatures and that this temperature (indicated by black arrows) increases with increasing amount of non-stoichiometry in La-doped

SSO grown on LAO(001). Even the nominally stoichiometric films on LAO(001) showed a small resistivity upturn at  $T \approx 100$  K raising a question on the source of disorder in a nominally stoichiometric film. Before we discuss these data, let's turn to the transport results of nominally stoichiometric La-doped SSO(40 nm)/undoped SSO(8 nm)/GSO(110) revealing overall smaller  $\rho$  (shown by red open circles) with a significantly higher  $\mu \sim 55 \text{ cm}^2\text{V}^{-1}\text{s}^{-1}$  at  $n = \sim 5.7 \times 10^{19} \text{ cm}^{-3}$ . A similar resistivity upturn was observed in this sample but at a much lower temperature  $T \approx 45$  K. These results indicate lesser disorder and scattering in stoichiometric film on GSO(110) in addition to raising the same question on the origin of this upturn in nominally stoichiometric films. To this end, we performed RSM analysis of stoichiometric La-doped SSO(40 nm)/undoped SSO(8 nm)/GSO(110) revealing that these films are mostly strained with some relaxation (see Fig. S2)<sup>24</sup> whereas those grown on LAO(001) substrates were mostly relaxed (see Fig. 1c). These results suggest an important role of dislocations on low temperature electronic transport. It is also noteworthy that both dislocations and non-stoichiometry-related defects appear to raise the temperature at which resistivity upturn occurs suggesting dislocation cores may also be vacancy-like. Future studies should be directed towards examining the composition of dislocation cores.

We next discuss the origin of low temperature resistivity upturn. Figure 3a and 3d show  $\rho$  vs  $\ln T$  plots for the stoichiometric La-doped SSO(45 nm)/undoped SSO(9 nm)/LAO(001) and La-doped SSO(40 nm)/undoped SSO(8 nm)/GSO(110), respectively. Green solid lines represent fits corresponding to the Fermi liquid (FL) behavior,  $\rho = \rho_0 + AT^2$  indicating electron-electron scattering as the dominant scattering mechanism at high temperatures  $140 \text{ K} < T < 300 \text{ K}$  on both substrates. At low temperatures,  $\rho$  vs  $\ln T$  revealed a linear dependence (black solid lines), which can be attributed to the quantum corrections. These quantum corrections can be due to weak

localization (WL) or electron-electron interaction effects, both of which show a similar behavior and can co-exist.<sup>27</sup> Magnetic field (B) can be used to differentiate between these two effects, as WL results into a negative magnetoresistance (MR) and is a low B-field effect<sup>27</sup>, whereas electron-electron interaction yields positive MR and are usually dominant at higher B-fields.<sup>28</sup> The zero-field resistivity correction due to WL in the 2D case is given by<sup>27</sup>

$$\sigma(T) = \frac{1}{\rho(T)} = \sigma_o + p \frac{e^2}{\pi h} \ln \left[ \frac{T}{T_0} \right] \quad (1)$$

where  $T_0$  is the temperature where quantum corrections begin to dominate.  $\sigma_o$  is a residual conductivity and  $h$  is the Planck constant. The value of  $p$  depends on the dominant scattering mechanism. Black solid lines in Figure 3a and 3d represent a linear fit to the experimental data at low temperatures using equation 1 suggesting that 2D WL governs the transport behavior. These fittings also yielded a value of  $p$  to be 1.69 and 2.1 for stoichiometric film on LAO(001), and GSO(110) respectively. We will discuss the implications of these values later.

To examine whether low temperatures  $\rho$  is dominated by the WL or electron-electron interaction effect, we performed MR measurements as a function of temperature as shown in Fig. S3.<sup>24</sup> The MR of both samples shows negative values and its magnitude increases with decreasing temperature, indicating WL as the dominant effect. However, at higher B-field values, relative change in MR with B-field became smaller suggesting increased contribution from electron-electron interaction effect. For this reason, we used low B-field MR values (as illustrated in Fig. 3b, and 3e) to obtain further insights into the WL mechanism such as their dimensionality and phase coherence length of electrons ( $L$ ).

For 2D WL, normalized MR ( $\frac{\Delta R}{R^2}$ ) in the absence of spin-orbit coupling can be written as<sup>29</sup>:

$$\frac{\Delta R}{R^2} = \frac{R(B) - R(0)}{R(B)^2} = \frac{e^2}{2\pi^2 \hbar} \left[ \psi \left( \frac{1}{2} + \frac{1}{x} \right) - \ln \left( \frac{1}{x} \right) \right] \quad (2)$$

where,  $\psi$  is the digamma function; and  $x=4eBL^2/\hbar$  where  $B$  is magnetic field,  $L$  is the electron phase coherence length and  $\hbar$  is the reduced Planck constant. It is noteworthy that there is only one fitting parameter,  $L$  in this equation. Likewise, for the 3D WL, above expression is given by<sup>30</sup>:

$$\frac{\Delta R}{R^2} = \frac{e^2}{2\pi^2\hbar} \sqrt{\frac{eB}{\hbar}} \left[ 2 \left( \left(2 + \frac{1}{x}\right)^{1/2} - \left(\frac{1}{x}\right)^{1/2} \right) - \left(\frac{1}{2 + \frac{1}{x}}\right)^{-1/2} - \left(\frac{3}{2 + \frac{1}{x}}\right)^{-1/2} + \frac{1}{48} \left(2.03 + \frac{1}{x}\right)^{-3/2} \right] \quad (3)$$

We show in Fig. 3b and Fig. 3e the low B-field experimental data and WL fits for the stoichiometric La-doped SSO on LAO(001), and GSO(110) respectively. We first discuss the data from La-doped SSO(45 nm)/undoped SSO(9 nm)/LAO(001) in Fig. 3b, which shows experimental data (symbols) and fits using both 2D WL (solid black line, equation 2) and 3D WL models (black dashed line, equation 3). The 2D WL can describe the experimental MR behavior reasonably well for  $1.8 \text{ K} \leq T \leq 25 \text{ K}$ , but fails at higher temperatures,  $25 \text{ K} \leq T \leq 100 \text{ K}$ . High-temperature data, on the other hand, can be explained using 3D WL model. Notably, the temperature where there is a crossover from 2D to 3D WL is also consistent with the deviation of linearity in  $\rho$  vs  $\ln T$  as illustrated in Fig. 3a. The extracted values of  $L$  from these fittings are shown in Fig. 3c as a function of temperature. The horizontal dotted line corresponds to the doped layer thickness of 45 nm again corroborating with our findings of dimensional crossover at  $T \approx 25 \text{ K}$ . It is expected that  $T$ -dependence of  $L$  scales as  $T^{-p/2}$  where the value of  $p$  can allow for determining the types of scattering mechanisms, i.e.  $p = 1.0$  and  $1.5$  for inelastic electron-electron scattering in 2D and 3D regime, respectively.<sup>31</sup> As illustrated in Fig. 3c, analysis of the data yielded a value of  $p$  equal to 0.96 in the 2D regime, consistent with electron-electron scattering. Since we only have limited data points in the 3D WL regime to correctly determine the value of  $p$ , we can only comment that an increase in the slope is suggestive of electron-

electron scattering being the dominant scattering mechanism in the 3D regime as well. We now turn to the discussion of stoichiometric La doped SSO(40 nm)/undoped SSO(8 nm)/GSO(110) as illustrated in Fig. 3e and 3f. Figure 3e shows  $\frac{\Delta R}{R^2}$  vs  $B$  plots for  $1.8 \text{ K} \leq T \leq 50 \text{ K}$  revealing excellent agreement between experimental data and 2D WL fits using equation 2. This result is further consistent with the observation of linear behavior in  $\rho$  vs  $\ln T$  plot as illustrated in Fig. 3a. The extracted values of  $L$  from these MR fittings are shown in Fig. 3f as a function of temperature. Doped layer thickness, 40 nm, is labeled by the dashed line in agreement with the observed behavior of 2D WL at  $T < 50 \text{ K}$ . The  $L$  shows  $T^{-0.58}$  dependence yielding a value of  $p = 1.16$ , indicating inelastic electron-electron scattering as the dominant scattering mechanism. Clearly, the value of  $p$  determined from MR analysis and those from the analysis of low temperature  $\rho$  vs  $\ln T$  differ significantly. We attribute this difference to the presence of electron-electron interaction effect at low temperatures, which is not accounted for in equation 1. This effect can also be noticed in Fig. 3f showing a saturation in the value of  $L$  at  $T < 5\text{K}$ .<sup>32</sup>

Notably, the comparison of  $L$  between these two samples using different substrates suggests that the presence of large density of dislocation in La-doped SSO on LAO lead to a decrease in the value of  $L$  and therefore results in a dimensional crossover from 2D to 3D WL. To further investigate this point, we show in Fig. S4 transport results from La-doped SSO on LAO(001) grown intentionally with non-stoichiometric composition (Sr:Sn ratio = 1.08), i.e. with increased disorder and are thus expected to have wider 3D WL regime as a function of temperature.<sup>24</sup> Figure S4 shows consistent results revealing that 2D to 3D WL crossover (Fig. S4)<sup>24</sup> occurs at a lower temperature accompanied by an expanded region for 3D WL when disorder is increased. These results are consistent with the findings of decreased electron phase coherence length due to the presence of disorder associated with both dislocations and point

defects. A similar behavior has been previously reported in ZnO/TiO<sub>x</sub> heterostructure<sup>33</sup>, n-GaAs<sup>34</sup> owing to the presence of disorder.

Finally, to address the question of what governs the transport in a highly non-stoichiometric sample, we show in Fig. 4a the semi-log plot of the zero-field  $\rho$  versus  $T^{-1/4}$  of a representative La-doped SSO/LAO(001) with Sr/Sn RBS ratio of  $0.93 \pm 0.02$ . The inset shows Zabrodskii and Zinov'eva analysis<sup>35</sup>, an unbiased quantitative technique that compares reduced activation energy  $\left( W = -d(\ln \rho) / d(\ln T) \right)$  vs  $T$  on a double logarithmic plot. The calculated slope ( $m$ ) of this curve using least square fit reveals a value of  $-0.24 \pm 0.01$  indicating the Mott 3D variable range hopping (VRH) is at play at low temperature  $T < 10$  K. This result is consistent with the strong positive contribution to the measured MR values at high magnetic field<sup>36, 37</sup> (Fig. 4b). With increasing  $T$ , MR transitioned to negative values at all magnetic fields,  $-9 \text{ T} \leq B \leq +9 \text{ T}$ . In the context of hopping transport, the positive MR at high magnetic field can be understood due to the shrinkage of the localized orbital wave function reducing the probability of the overlap between the localized states. In relatively weak magnetic fields, a negative contribution to the MR is due to the suppression of destructive interference between the forward scattering hopping paths<sup>38</sup>. The temperature dependence suggests that sample undergoes a weakly-localized to a strongly-localized transport with decreasing temperature.

### **Conclusions:**

In summary, we have demonstrated the hybrid MBE approach for the growth of phase-pure, stoichiometric, epitaxial SSO films in layer-by-layer growth mode. The use of highly volatile HMDT precursor facilitated adsorption-controlled growth of SSO with self-regulating cation stoichiometry and yielded record-high room temperature mobility of  $55 \text{ cm}^2\text{V}^{-1}\text{s}^{-1}$  in La-doped

films on GSO(110). Non-stoichiometry-related defects resulted in lower mobility and a crossover from weak to strong localization of carriers, irrespective of whether they were Sr- or Sn-vacancies. Substrate-induced dislocations in doped-SSO films on LAO(001) yielded dimensional crossover from 2D to 3D WL behaviors. Future investigations on mobility optimization in these materials should account for the disorder caused by the presence of non-stoichiometry as well as dislocations.

### **Acknowledgements:**

This work was primarily supported by National Science Foundation through DMR-1741801, 1607318, 1410888 and partially by the UMN MRSEC program under Award Number DMR-1420013. The part of this work was supported through the Young Investigator Program of the Air Force Office of Scientific Research (AFOSR) through Grant FA9550-16-1-0205. The work also acknowledges partial support from the RDF Fund of the Institute on the Environment (UMN). Parts of this work were carried out at the Minnesota Nano Center and Characterization Facility, University of Minnesota, which receives partial support from NSF through the MRSEC program. T.W. and A.P. would like to acknowledge the support from the UMN Doctoral Dissertation Fellowship.

### **References:**

1. H. J. Kim, U. Kim, H. M. Kim, T. H. Kim, H. S. Mun, B.-G. Jeon, K. T. Hong, W.-J. Lee, C. Ju, K. H. Kim and K. Char, *Appl. Phys. Exp.* **5**, 061102 (2012).
2. X. Luo, Y. S. Oh, A. Sirenko, P. Gao, T. A. Tyson, K. Char and S.-W. Cheong, *Appl. Phys. Lett.* **100**, 172112 (2012).
3. K. Krishnaswamy, L. Bjaalie, B. Himmetoglu, A. Janotti, L. Gordon and C. G. V. d. Walle, *Appl. Phys. Lett.* **108**, 083501 (2016).
4. S. A. Chambers, T. C. Kaspar, A. Prakash, G. Haugstad and B. Jalan, *Appl. Phys. Lett.* **108**, 152104 (2016).

5. S. I. Beigi, F. J. Walker, S. W. Cheong, K. M. Rabe and C. H. Ahn, *APL Mater.* **3**, 062510 (2015).
6. W. J. Lee, H. J. Kim, J. Kang, D. H. Jang, T. H. Kim, J. H. Lee and K. H. Kim, *Annu. Rev. Mater. Res.* **47**, 391 (2017).
7. S. Raghavan, T. Schumann, H. Kim, J. Y. Zhang, T. A. Cain and S. Stemmer, *APL Mater.* **4**, 016106 (2016).
8. Z. L. Higgins, D. O. Scanlon, H. Paik, S. Sallis, Y. Nie, M. Uchida, N. F. Quackenbush, M. J. Wahila, G. E. Sterbinsky, D. A. Arena, J. C. Woicik, D. G. Schlom and L. F. J. Piper, *Phys. Rev. Lett.* **116**, 027602 (2016).
9. A. Prakash, P. Xu, A. Faghaninia, S. Shukla, J. W. A. III, C. S. Lo and B. Jalan, *Nat. Commun.* **8**, 15167 (2017).
10. H. J. Kim, U. Kim, T. H. Kim, J. H. Kim, H. M. Kim, B.-G. Jeon, W.-J. Lee, H. S. Mun, K. T. Hong, J. Yu, K. Char and K. H. Kim, *Phys. Rev. B* **86** (16), 165205 (2012).
11. K. Ganguly, P. Ambwani, P. Xu, J. S. Jeong, K. A. Mkhoyan, C. Leighton and B. Jalan, *APL Mater.* **3**, 062509 (2015).
12. T. Schumann, S. Raghavan, K. Ahadi, H. Kim and S. Stemmer, *J. Vac. Sci. Technol., A* **34**, 050601 (2016).
13. B. Bellal, B. Hadjarab, A. Bouguelia and M. Trari, *Theor. Exp. Chem.* **45**, 172 (2009).
14. D. J. Singh, Q. Xu and K. P. Ong, *Appl. Phys. Lett.* **104**, 011910 (2014).
15. K. P. Ong, X. Fan, A. Subedi, M. B. Sullivan and D. J. Singh, *APL Mater.* **3**, 062505 (2015).
16. H. R. Liu, J. H. Yang, H. J. Xiang, X. G. Gong and S. H. Wei, *Appl. Phys. Lett.* **102**, 112109 (2013).
17. K. Nomura, S. Suzuki, Y. Koike, H. Li, A. Okazawa and N. Kojima, *Hyperfine Interact.* **237**, 26 (2016).
18. Q. Liu, J. Dai, X. Zhang, G. Zhu, Z. Liu and G. Ding, *Thin Sol. Films* **519**, 6059 (2011).
19. M. C. F. Alves, S. Boursicot, S. Ollivier, V. Bouquet, S. Deputier, A. Perrin, I. T. Weber, A. G. Souza, I. M. G. Santos and M. G. Viry, *Thin Sol. Films* **519**, 614 (2010).
20. H. M. Christen, L. A. Boatner, J. D. Budai, M. F. Chisholm, L. A. Gea, D. P. Norton, C. Gerber and M. Urbanik, *Appl. Phys. Lett.* **70**, 2147 (1997).
21. L. Qinzhuang, L. Hong, L. Bing, W. Wei, L. Qiangchun, Z. Yongxing and D. Jianming, *Europhys. Lett.* **108**, 37003 (2014).
22. G. Prathiba, S. Venkatesh, K. K. Bharathi and H. Kumar, *J. Appl. Phys.* **109**, 07C320 (2011).
23. I. R. Shein, V. L. Kozhevnikov and A. L. Ivanovskii, *Solid State Sci.* **10**, 217 (2008).
24. See Supplemental Material at [URL will be inserted by publisher] for the description of experimental methods, Rutherford backscattering spectrometry, X-ray reciprocal space map, and magnetoresistance measurements of SSO films.
25. A. Prakash, P. Xu, X. Wu, G. Haugstad, X. Wang and B. Jalan, *J. Mater. Chem. C* **5**, 5730 (2017).
26. D. O. Scanlon, *Phys. Rev. B* **87**, 161201 (2013).
27. P. A. Lee and T. V. Ramakrishnan, *Rev. Mod. Phys.* **57**, 287 (1985).
28. B. L. Altshuler, A. G. Aronov and P. A. Lee, *Phys. Rev. Lett.* **44**, 1288 (1980).
29. C. V. Haesendonck, L. V. d. dries and Y. Bruynseraede, *Phys. Rev. B* **25**, 5090 (1982).
30. D. V. Baxter, R. Richter, M. L. Trudeau, R. W. Cochrane and J. O. Stromolsen, *J. Phys. France* **50**, 1673 (1989).
31. E. Akkermans and G. Montambaux, *Mesoscopic Physics of Electrons and Photons*. (Cambridge University Press 2007).

32. J. J. Lin and J. P. Bird, *J. Phys. Condens. Matter* **14**, R501 (2002).
33. D. Saha, P. Misra, S. Bhartiya, M. Gupta, M. P. Joshi and L. M. Kukreja, *Appl. Phys. Lett.* **108**, 042109 (2016).
34. A. M. Gilbertson, A. K. M. Newaz, W. J. Chang, R. Bashir, S. A. Solin and L. F. Cohen, *Appl. Phys. Lett.* **95**, 012113 (2009).
35. A. G. Zabrodskii and K. N. Zinoveva, *JETP Letters* **37**, 436 (1983).
36. M. E. Gershenson, Y. B. Khavin, A. G. Mikhalchuk, H. M. Bozler and A. L. Bogdanov, *Phys. Rev. Lett.* **79**, 725 (1997).
37. G. M. Minkov, A. V. Germanenko, O. E. Rut, A. A. Sherstobitov and B. N. Zvonkov, *Phys. Rev. B* **75**, 235316 (2007).
38. B. I. Shklovskii and B. Z. Spivak, *Hopping transport in solids*. (Elsevier, 1991).

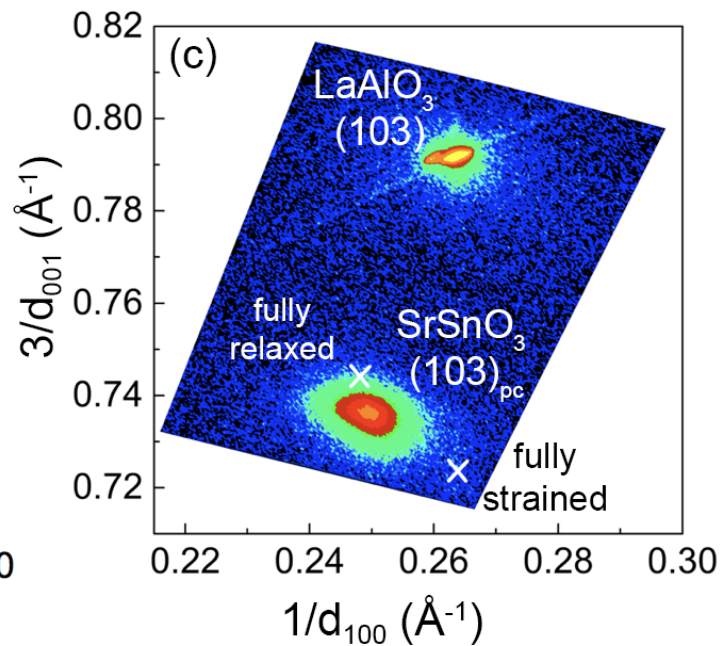
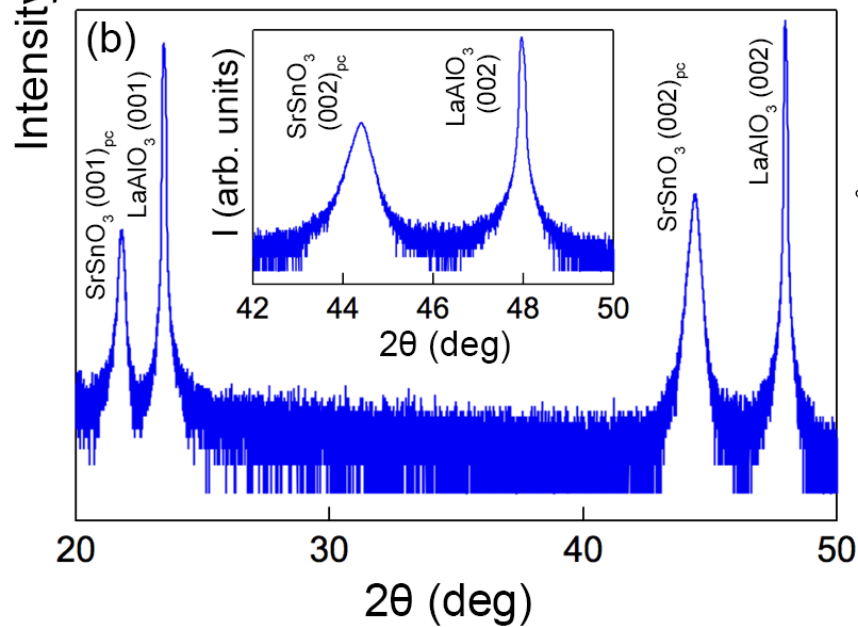
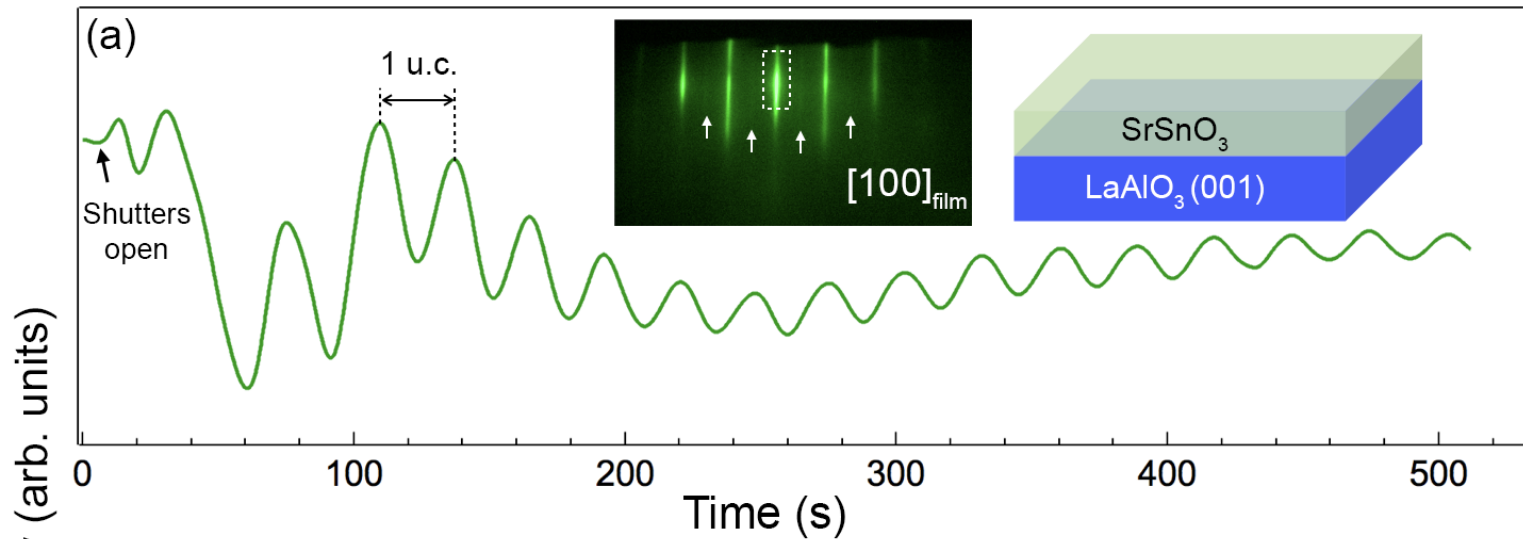
## Figure Captions:

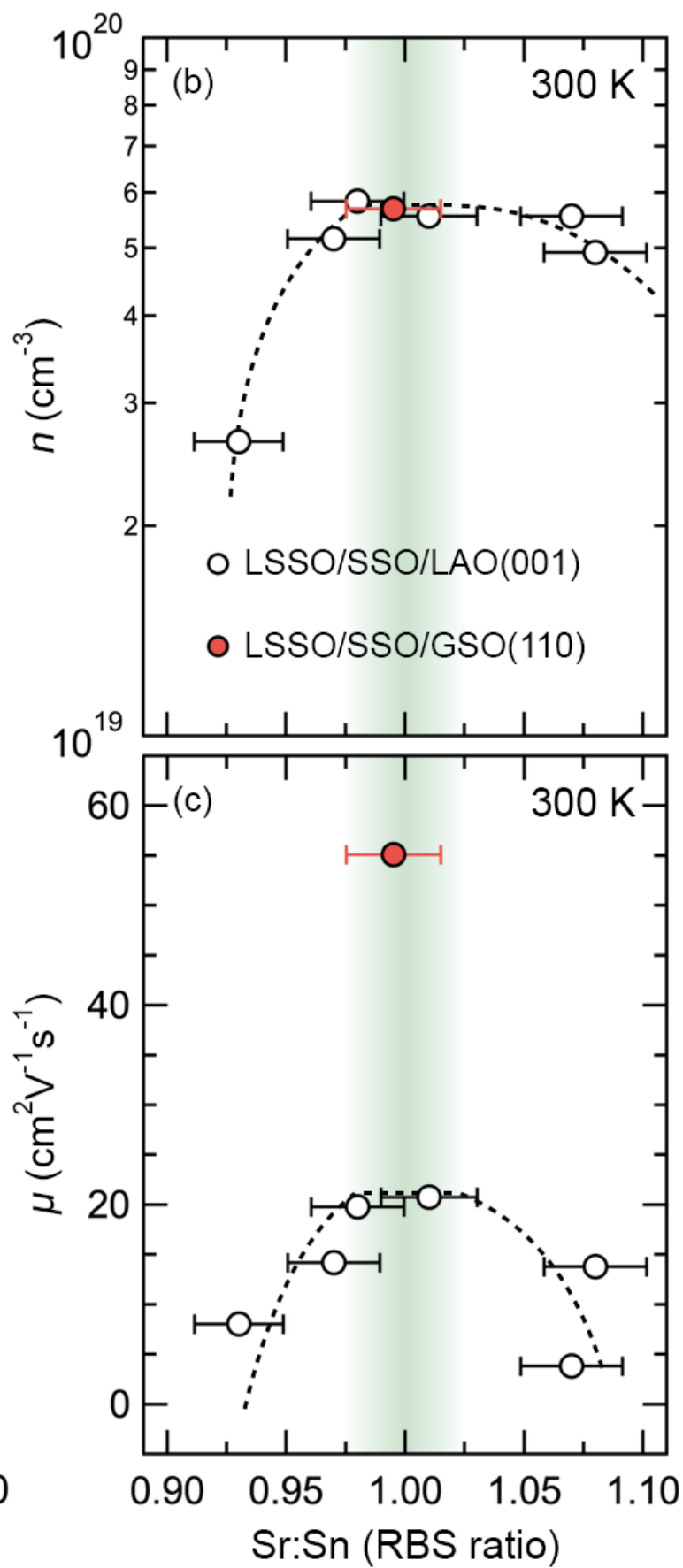
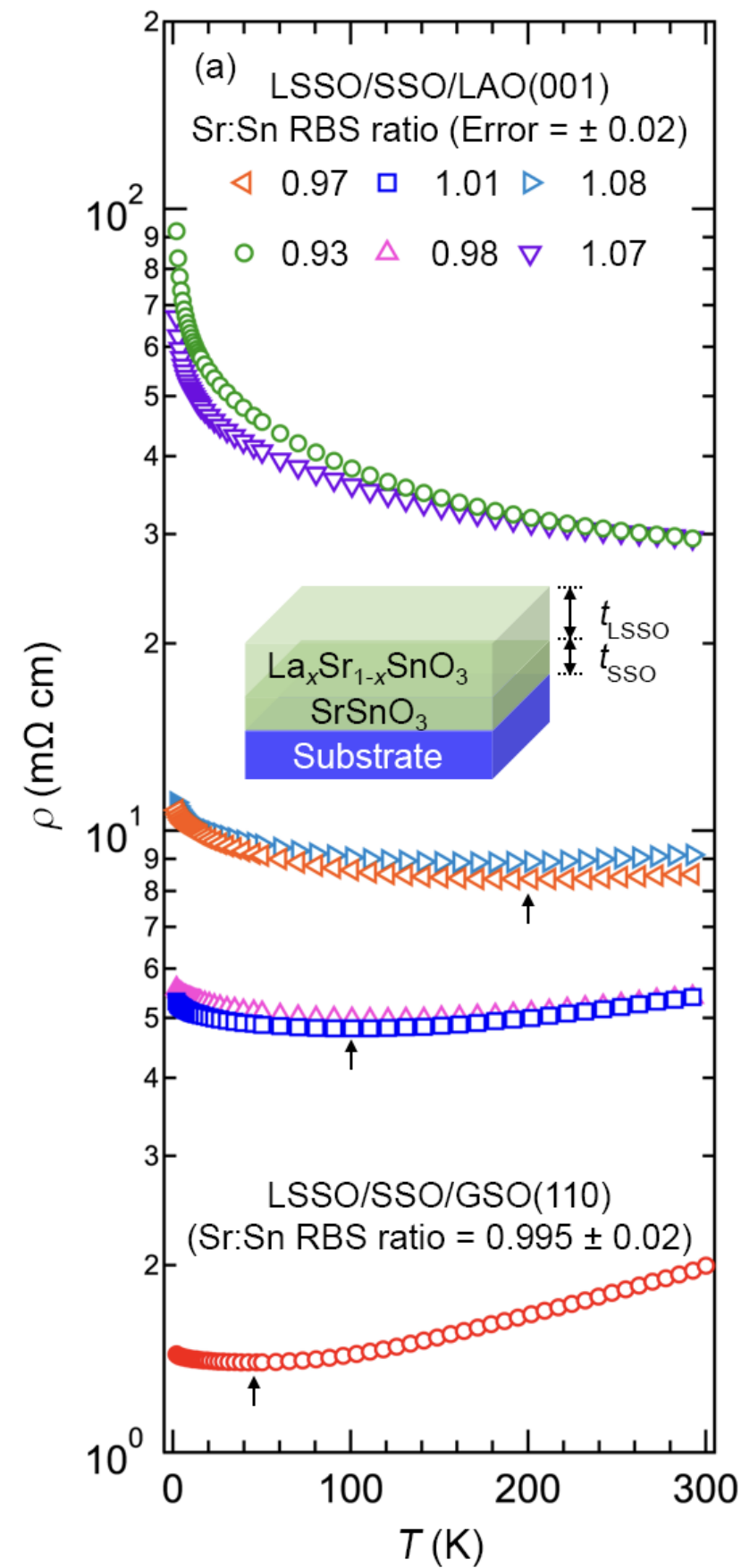
**Figure 1:** (a) Time-dependent RHEED intensity oscillations for SSO film grown on LAO(001) substrate grown at a Sr:Sn BEP ratio of  $8.6 \times 10^{-3}$ . The insets show the RHEED pattern along the  $[100]_{\text{LAO}}$  azimuth after growth, and a schematic of film structure. (b) High-resolution x-ray diffraction for a La-doped SSO(45 nm)/undoped SSO(9 nm)/LAO (001) with an inset showing a close up around the  $(002)_{\text{pc}}$  film/substrate peaks. (c) Off-axis RSM taken around (103) reflection of SSO film on LAO(001). Cross symbol marks the expected positions of a fully strained and a fully relaxed SSO film on LAO(001).

**Figure 2:** (a)  $\rho$  vs  $T$  for La-doped SSO (40 nm)/undoped SSO (8 nm)/GSO(110) and La-doped SSO(45 nm)/undoped SSO(9 nm)/LAO(001) as a function of Sr/Sn ratio determined from the RBS measurements. Inset shows a schematic of the sample structure. (b)  $n$  and (c)  $\mu$  measured at 300 K as a function of Sr/Sn RBS ratio.

**Figure 3:** (a, d)  $\rho$  vs  $\ln T$  for stoichiometric films grown on LAO(001) and GSO(110), respectively. Black solid lines are the linear fits using equation 1, whereas the green solid lines are fits using the Fermi liquid model. (b, e) Normalized MR (symbols) as a function of magnetic field at different temperatures for the same films showing the WL fits with solid lines representing fits using 2D WL model whereas dashed lines are fits using 3D WL model. (c, f) Temperature dependence of the electron phase coherence length along with the linear fits for films grown on LAO(001) and GSO(110) respectively. The horizontal dashed lines in (c and f) indicate the active layer thickness of SSO films.

**Figure 4:** (a) Logarithmic resistivity versus  $T^{-1/4}$  plot for the most non-stoichiometric film (Sr/Ba RBS ratio =  $0.93 \pm 0.02$ ) grown on LAO(001). The solid black line is the linear fit using the Mott 3D VRH model. Inset shows the temperature dependence of the reduced activation energy using Zabrodskii and Zinov'eva analysis, yielding a slope,  $m = -0.24 \pm 0.01$  indicating the Mott 3D VRH behavior. (b) MR data of the same sample as a function of temperature.

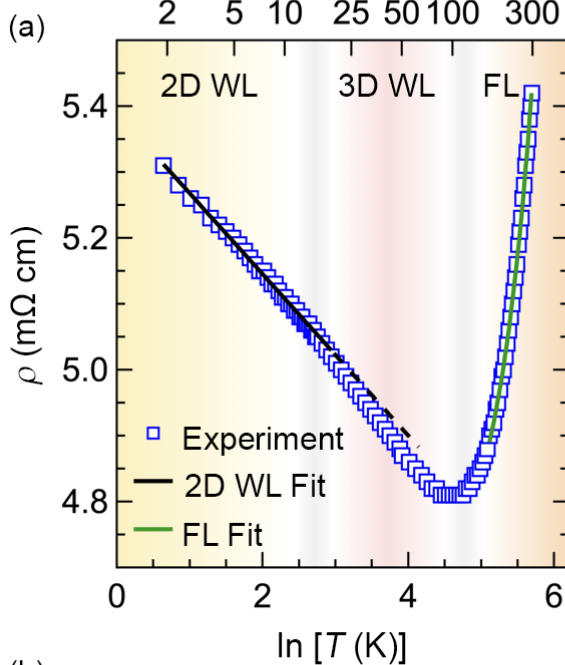




LSSO/SSO/LAO(001)  
(Sr:Sn RBS ratio =  $1.01 \pm 0.02$ )

$T$  (K)

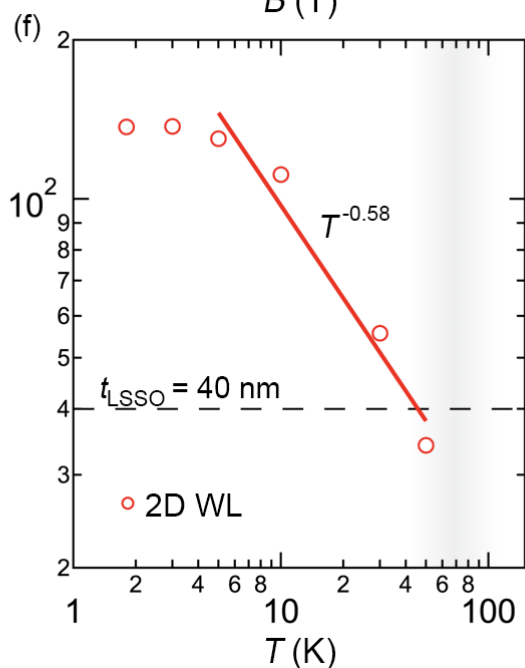
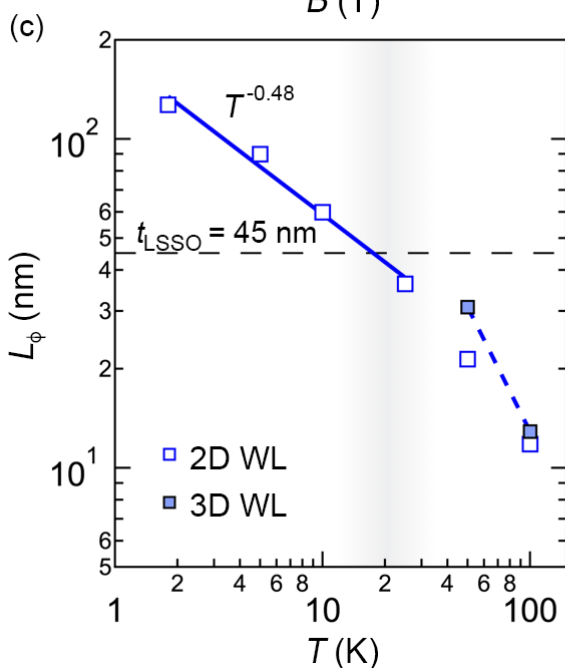
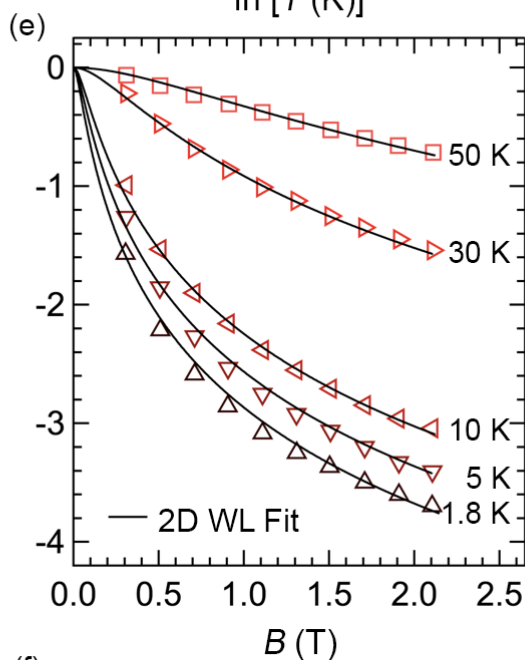
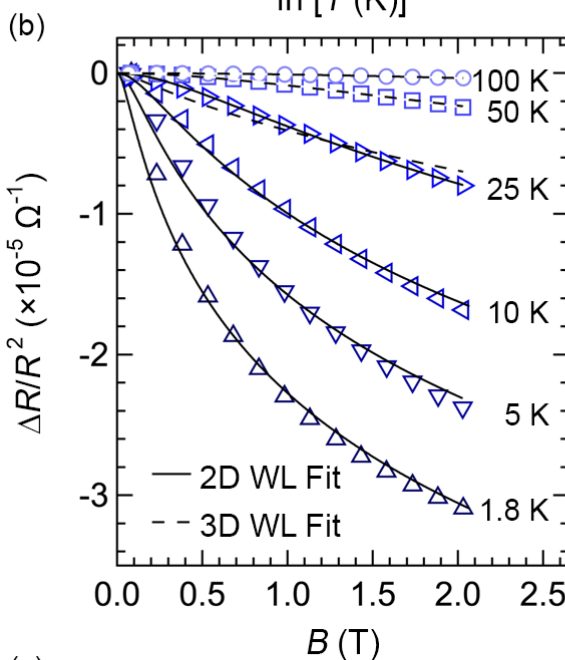
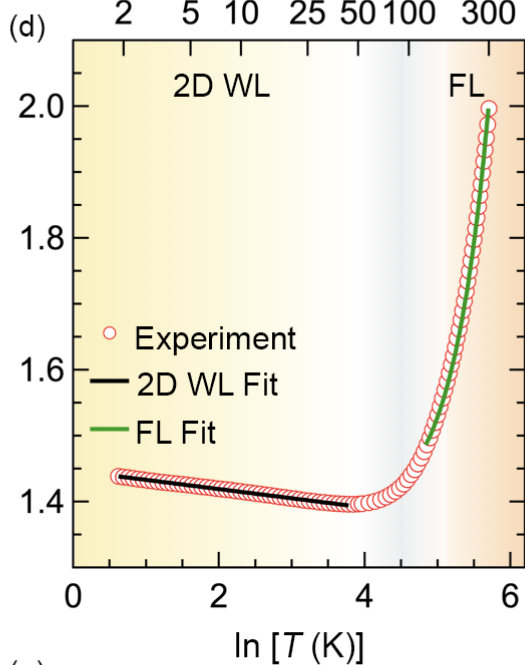
2 5 10 25 50 100 300



LSSO/SSO/GSO(110)  
(Sr:Sn RBS ratio =  $0.995 \pm 0.02$ )

$T$  (K)

2 5 10 25 50 100 300



LSSO/SSO/LAO(001)  
(Sr:Sn RBS ratio =  $0.93 \pm 0.02$ )

